Electrical Properties Tomography Using Contrast Source Inversion Techniques

R .F. Remis* A. Webb† S. Mandija‡ R. L. Leijsen† P. S. Fuchs*
P. R. S. Stijnman* C. A. T. van den Berg‡

Abstract — **In this paper, we present an Electrical Properties Tomography (EPT) methodology based on integral (Green's tensor) representations for the electromagnetic field. Inhomogeneous tissue profiles can easily be incorporated in such an approach and the reconstruction method is less sensitive to noise compared with more standard differential based EPT methods since smoothing integral operators act on measured field data. To keep the computational bookkeeping to a minimum, we derive our basic EPT field representations for two-dimensional E-polarized radio frequency fields, which is a valid assumption in the midplane of a loaded birdcage coil. The extension to the fully three-dimensional case is briefly discussed and some initial 3D reconstructions are presented as well. Possible extensions and practical implementation issues are also discussed.**

1 INTRODUCTION

In Electrical Properties Tomography (EPT), the objective is to retrieve the dielectric parameters (conductivity and permittivity) of different tissue types from transmit magnetic field (B_1^+) data measured at the MRI Larmor frequency. In this paper, we present a general Contrast Source Inversion (CSI) framework to solve this EPT problem. As opposed to more common local differential-based EPT methods that work directly on measured B_1^+ data [1] – [6], and are thus very susceptible to noise, we take the global integral (Green's tensor) representations for the fields as a starting point. These integral representations express the radio frequency field in terms of a dielectric contrast source (due to the presence of the human body) and are less sensitive to noise, since integral rather than differential operators act on the measured data. Furthermore, by using this approach we also circumvent problems related to the accurate determination of spatial derivatives at tissue boundaries, and varying tissue contrasts can be taken into account in a straightforward manner, thereby facilitating more accurate reconstructions at tissue boundaries. In our CSI approach, tissue parameters are obtained by iteratively minimising a properly defined cost functional that measures the discrepancy between measured and modeled B_1^+ data (data mismatch) and the discrepancy in satisfying Maxwell's equations (state mismatch). We are also able to simultaneously reconstruct the electric field strength that corresponds to the measured B_1^+ field, which enables estimation of the Specific Absorption Rate (SAR). We formulate our global CSI method for B_1^+ field data acquired within the midplane of a birdcage coil. The RF field within this plane is essentially two-dimensional and E-polarized, and therefore computationally less expensive two-dimensional field integral representations can be used. We also present reconstruction results for fully vectorial 3D CSI-EPT, which is not restricted to the midplane of a birdcage coil, and demonstrate that CSI-EPT can in principle handle large spatial jumps in the dielectric tissue profiles.

2 INTEGRAL REPRESENTATIONS

In the midplane of a birdcage coil, the electromagnetic field is essentially two-dimensional and E-polarized in the z-direction with the z-axis coinciding with the central axis of the coil. Using an $\exp(\mathrm{j}\omega t)$ time convention, this radio frequency field satisfies the Maxwell equations

$$-\partial_x \hat{B}_y + \partial_y \hat{B}_x + \mu_0 \hat{J}_z^{\mathrm{ind}} = 0, \tag{1}$$

$$\partial_y \hat{E}_z + \mathrm{j}\omega \hat{B}_x = 0, \tag{2}$$

and

$$-\partial_x \hat{E}_z + \mathrm{j}\omega \hat{B}_y = 0, \tag{3}$$

inside the body slice located in the midplane of the birdcage coil, where the frequency of operation $\omega = \omega_0$ is the Larmor frequency, and

$$\hat{J}_z^{\mathrm{ind}} = (\sigma + \mathrm{j}\omega\varepsilon)\hat{E}_z \tag{4}$$

is the induced electric current density with σ and ε the conductivity and permittivity tissue profiles of the body in the midplane of the birdcage coil.

*Circuits and Systems Group, Delft University of Technology, Delft, The Netherlands, e-mail: R.F.Remis@tudelft.nl, P.S.Fuchs@tudelft.nl, P.R.S.Stijnman@student.tudelft.nl.

†Gorter Center for High Field MRI, Leiden University Medical Center, The Netherlands, e-mail: A.Webb@lumc.nl, R.L.Leijsen@lumc.nl.

‡Imaging Division, University Medical Center Utrecht, The Netherlands, e-mail: S.Mandija@umcutrecht.nl, C.A.T.vandenBerg@umcutrecht.nl.

978-1-5090-4451-1/17/$31.00 ©2017 IEEE

To arrive at the integral representations used in our EPT method, we set up a scattering formalism and write the electromagnetic field as

$$\hat{E}_z = \hat{E}_z^{\mathrm{b}} + \hat{E}_z^{\mathrm{sc}}, \tag{5}$$

$$\hat{B}_x = \hat{B}_x^{\mathrm{b}} + \hat{B}_x^{\mathrm{sc}}, \tag{6}$$

and

$$\hat{B}_y = \hat{B}_y^{\mathrm{b}} + \hat{B}_y^{\mathrm{sc}}, \tag{7}$$

where $\{\hat{E}_z^{\mathrm{b}}, \hat{B}_x^{\mathrm{b}}, \hat{B}_y^{\mathrm{b}}\}$ is the background radio frequency field in the absence of the human body, while $\{\hat{E}_z^{\mathrm{sc}}, \hat{B}_x^{\mathrm{sc}}, \hat{B}_y^{\mathrm{sc}}\}$ is the scattered field due to the presence of the human body that occupies the bounded domain $\mathbb{D}_{\mathrm{body}}$ in the transverse midplane of the birdcage coil.

With $\boldsymbol{\rho}$ the position vector in the transverse xy-plane, the background electric field is given by

$$\hat{E}_z^{\mathrm{b}}(\boldsymbol{\rho}) = -\mathrm{j}\omega\mu_0 \int_{\boldsymbol{\rho}' \in \mathbb{D}_{\mathrm{src}}} \hat{G}(\boldsymbol{\rho}, \boldsymbol{\rho}') \hat{J}_z^{\mathrm{ext}}(\boldsymbol{\rho}') \, \mathrm{d}A, \tag{8}$$

where $\hat{J}_z^{\mathrm{ext}}$ is the external (impressed) current density running along the z-direction in the rungs of the birdcage coil with support $\mathbb{D}_{\mathrm{src}}$ in the xy-plane and $\hat{G}$ is the Green's function of the background configuration with or without the RF shield. The former case has computational advantages and the presence of the RF shield can approximately be taken into account via mirror sources (see [7]). For completeness, we mention that as soon as the background electric field strength has been determined via Eq. (8), the background magnetic flux density follows from Maxwell's equations as

$$\hat{B}_x^{\mathrm{b}} = -\frac{1}{\mathrm{j}\omega}\partial_y \hat{E}_z^{\mathrm{b}} \quad \text{and} \quad \hat{B}_y^{\mathrm{b}} = \frac{1}{\mathrm{j}\omega}\partial_x \hat{E}_z^{\mathrm{b}} \tag{9}$$

and the background B_1^+ field is obtained as

$$\hat{B}_1^{+;\mathrm{b}} = \frac{\hat{B}_x^{\mathrm{b}} + \mathrm{j}\hat{B}_y^{\mathrm{b}}}{2} = \frac{1}{2\omega}\bar{\partial}\hat{E}_z^{\mathrm{b}}, \tag{10}$$

where we have introduced the del-bar operator

$$\bar{\partial} = \partial_x + \mathrm{j}\partial_y. \tag{11}$$

Furthermore, for the scattered electric field strength we have the integral representation

$$\hat{E}_z^{\mathrm{sc}}(\boldsymbol{\rho}) = -\mathrm{j}\omega\mu_0 \int_{\boldsymbol{\rho}' \in \mathbb{D}_{\mathrm{body}}} \hat{G}(\boldsymbol{\rho}, \boldsymbol{\rho}') \hat{J}_z^{\mathrm{sc}}(\boldsymbol{\rho}') \, \mathrm{d}A, \tag{12}$$

where the electric scattering source is given by

$$\hat{J}_z^{\mathrm{sc}}(\boldsymbol{\rho}) = \begin{cases} \mathrm{j}\omega\varepsilon_0\chi(\boldsymbol{\rho})\hat{E}_z(\boldsymbol{\rho}) & \text{for } \boldsymbol{\rho} \in \mathbb{D}_{\mathrm{body}} \\ 0 & \text{for } \boldsymbol{\rho} \notin \mathbb{D}_{\mathrm{body}} \end{cases} \tag{13}$$

with a contrast function χ given by

$$\chi(\boldsymbol{\rho}) = \varepsilon_{\mathrm{r}}(\boldsymbol{\rho}) - 1 + \frac{\sigma(\boldsymbol{\rho})}{\mathrm{j}\omega\varepsilon_0}. \tag{14}$$

Note that the relative permittivity determines the real part of this function, while the conductivity determines its imaginary part.

Substituting the scattering source in the integral representation of Eq. (12), we obtain

$$\hat{E}_z(\boldsymbol{\rho}) = \hat{E}_z^{\mathrm{b}}(\boldsymbol{\rho}) + \mathcal{G}_{\mathrm{D}}\{\hat{w}\}(\boldsymbol{\rho}), \tag{15}$$

where we have introduced the object operator

$$\mathcal{G}_{\mathrm{D}}\hat{w} = k_0^2 \int_{\boldsymbol{\rho}' \in \mathbb{D}_{\mathrm{body}}} \hat{G}(\boldsymbol{\rho}, \boldsymbol{\rho}')\hat{w}(\boldsymbol{\rho}') \, \mathrm{d}A, \tag{16}$$

with k_0 the wave number of the background and

$$\hat{w}(\boldsymbol{\rho}) = \chi(\boldsymbol{\rho})\hat{E}_z(\boldsymbol{\rho}) \tag{17}$$

the contrast source. Finally, the scattered magnetic flux density is related to the scattered electric field strength via the Maxwell equations

$$\hat{B}_x^{\mathrm{sc}} = -\frac{1}{\mathrm{j}\omega}\partial_y \hat{E}_z^{\mathrm{sc}} \quad \text{and} \quad \hat{B}_y^{\mathrm{sc}} = \frac{1}{\mathrm{j}\omega}\partial_x \hat{E}_z^{\mathrm{sc}} \tag{18}$$

from which it follows that the scattered B_1^+ field is given by

$$\hat{B}_1^{+;\mathrm{sc}} = \frac{\hat{B}_x^{\mathrm{sc}} + \mathrm{j}\hat{B}_y^{\mathrm{sc}}}{2} = \frac{1}{2\omega}\bar{\partial}\hat{E}_z^{\mathrm{sc}}. \tag{19}$$

Substituting the integral representation of Eq. (15) in the above equation, we arrive at the data equation

$$\hat{B}_1^{+;\mathrm{sc}}(\boldsymbol{\rho}) = \mathcal{G}_{\mathrm{S}}^+\hat{w}, \tag{20}$$

where we have introduced the data operator

$$\mathcal{G}_{\mathrm{S}}^+\hat{w} = \frac{1}{2\omega}\bar{\partial}\,\mathcal{G}_{\mathrm{D}}\hat{w}. \tag{21}$$

3 EPT RECONSTRUCTION METHODS

In this section, we describe various reconstruction methods based on the integral representations presented above. We start with the method proposed in [8]. Here, an approximate contrast source $\hat{w}$ is determined from Eq. (20) through a deconvolution procedure. This procedure requires apodization, however, since deconvolution is an inherently unstable process in general. As soon as an approximate contrast source is found, the conductivity and permittivity profiles are determined with the help of an additional experiment using a homogeneous phantom model.

The method proposed in [9] also takes Eq. (20) as a starting point, but does not use any apodization and an additional phantom experiment is not required. Specifically, in this method first an approximate contrast function $\hat{w}$ is found by minimizing the discrepancy between the measured B_1^+ field (left-hand side of Eq. (20)) and the modeled field (right-hand side of Eq. (20)) using a properly defined objective function. Having found the contrast function $\hat{w}$, we substitute this function in Eq. (15) to obtain the electric field strength within the body. Since now both the contrast source $\hat{w}$ and the electric field $\hat{E}_z$ are known, the conductivity and permittivity maps follow from Eq. (17). Note that this method allows us to reconstruct the Specific Absorption Rate (SAR) as well, since the electric field strength is also reconstructed in this method.

In the Contrast Source Inversion EPT method (CSI-EPT) proposed in [10], the discrepancy in satisfying the data equation (20) and the state or object equation (15) is simultaneously minimized using a single objective function that depends on the contrast source and the contrast function. Both quantities are updated in an iterative fashion in CSI-EPT until the objective function falls below a user specified error tolerance. Upon convergence, a reconstructed contrast source and contrast function are computed from which the electric field strength can be determined as well using Eq. (17). The reconstruction results presented in [10] are all for two-dimensional tissue profiles located in the midplane of a body coil. Recently, we have extended 2D CSI-EPT to the fully three-dimensional case. As an illustration, in Fig. 1 we show the magnitude of the reconstructed contrast function of the Ella head model (2.5 mm grid, IT'IS foundation [11]) obtained via our 3D CSI-EPT algorithm and based on ideal volumetric B_1^+ data at 3T. The antenna setup consists of 16 finite length z-directed dipoles driven in quadrature mode with their centers equidistantly spaced apart on a circumferential circle with a diameter of 0.32 m. The measurement circle is located at the center z-slice of the head and from Fig. 1 we observe that reconstructions improve towards this center slice as the number of CSI-EPT iterations is increased.

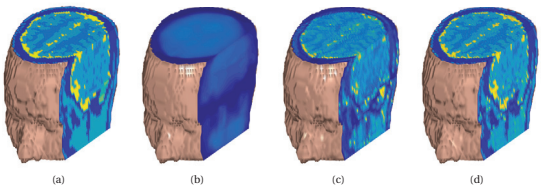

Figure 1: (a) Magnitude of original contrast function female head model. (b) Magnitude of the reconstructed contrast function after 100 iterations of 3D CSI-EPT. (c) Magnitude of the reconstructed contrast function after 1000 iterations of 3D CSI-EPT. (d) Magnitude of the reconstructed contrast function after 10000 iterations of 3D CSI-EPT.

4 DISCUSSION

Up to this point, we have assumed perfect B_1^+ data, meaning that the amplitude and phase of the B_1^+ field are exactly known. In practice, this is obviously not the case and the iterative reconstruction methods described above need to be adapted such that reliable reconstructions are obtained from measured B_1^+ field maps. These field maps are obtained by measuring the amplitude and the phase of the B_1^+ field in two different experiments and in each case the measurements are contaminated by noise. Therefore, noise suppressing techniques must be included in our reconstruction algorithms. The most obvious way to suppress the effects of noise in the reconstructions is to use the iteration number as a regularization parameter [12]. Much more advanced techniques, such as total variation [10], can be included as well, since we treat the EPT problem as an optimization problem, which we attempt to solve in an iterative manner. Furthermore, the phase of the measured B_1^+ field is perturbed by the phase of the B_1^- field and this perturbation has to be taken into account as well. One way to solve this problem is to apply the so-called transceive phase approximation [13], but the accuracy of this approximation is rather limited. Current research seems to indicate that, since we use iterative schemes to solve the EPT problem, the measured phase can be iteratively updated to correct for the B_1^- phase perturbations that are present in the phase measurements of the B_1^+ field. Finally, we point out that the magnitude of the electric field strength typically is very small around the center of a quadrature-driven birdcage coil. Generally, this has a negative impact on the conductivity and permittivity reconstructions in this region. Reconstructions around the center can be improved, however, through active or passive shimming [8] [10] or possibly by incorporating magnetic field strength representations in the optimization technique, or by including a priori information about the conductivity/permittivity profiles.

References

[1] E. Haacke, L. Petropoulos, E. Nilges, and D. Wu, "Extraction of conductivity and permittivity using magnetic resonance imaging,"

Physics in Medicine and Biology, Vol. 36, No. 6, p. 723, 1991.

[2] H. Wen, "Noninvasive quantitative mapping of conductivity and dielectric distributions using rf wave propagation effects in high-field MRI," in Medical Imaging 2003. International Society for Optics and Photonics, 2003, pp. 471 – 477.

[3] U. Katscher, T. Dorniok, C. Findeklee, P. Vernickel, and K. Nehrke, "In vivo determination of electric conductivity and permittivity using a standard mr system," in 13th International Conference on Electrical Bioimpedance and the 8th Conference on Electrical Impedance Tomography. Springer, 2007, pp. 508 – 511.

[4] D. K. Sodickson, L. Alon, C. M. Deniz, R. Brown, B. Zhang, G. C. Wiggins, G. Y. Cho, N. B. Eliezer, D. S. Novikov, R. Lattanzi, "Local maxwell tomography using transmit-receive coil arrays for contact-free mapping of tissue electrical properties and determination of absolute rf phase," in Proceedings of the 20th Annual Meeting of ISMRM, Melbourne, Australia, 2012, p. 387.

[5] X. Zhang, P.-F. V. de Moortele, S. Schmitter, and B. He, "Complex b1 mapping and electrical properties imaging of the human brain using a 16-channel transceiver coil at 7T," Magnetic Resonance in Medicine, Vol. 69, No. 5, pp. 1285 – 1296, 2013.

[6] J. Liu, X. Zhang, S. Schmitter, V. de Moortele, B. He, "Gradient-based electrical properties tomography (gept): A robust method for mapping electrical properties of biological tissues in vivo using magnetic resonance imaging," Magnetic resonance in medicine, Vol. 74, No. 3, pp. 634 – 646, 2015.

[7] J. Jin, "Electromagnetic Analysis and Design in Magnetic Resonance Imaging," CRC Press, 1999.

[8] R. Schmidt and A. Webb, "A new approach for electrical properties estimation using a global integral equation and improvements using high permittivity materials," Journal of Magnetic Resonance, Vol. 262, pp. 8 – 14, 2015.

[9] P. Fuchs, "Electric properties tomography using contrast source inversion," MSc Thesis, Delft University of Technology Repository, 2016.

[10] E. Balidemaj, C. A. T. van den Berg, J. Trinks, A. L. van Lier, A. J. Nederveen, L. J. Stalpers, H. Crezee, and R. F. Remis, "CSI-EPT: a contrast source inversion approach for improved MRI-based electric properties tomography," IEEE Transactions on Medical Imaging, Vol. 34, No. 9, pp. 1788 – 1796, 2015.

[11] A. Christ, W. Kainz, E. G. Hahn, "The virtual family development of surface-based anatomical models of two adults and two children for dosimetric simulations," Physics in Medicine and Biology, Vol. 55. pp. 23 – 38, 2010.

[12] B. Saleh, "Introduction to Subsurface Imaging," Cambridge University Press, 2011.

[13] A. L. Van Lier, D. O. Brunner, K. P. Pruessmann, D. W. Klomp, P. R. Luijten, J. J. Lagendijk, and C. A. T. van den Berg, "B_1^+ phase mapping at 7 T and its application for in vivo electrical conductivity mapping," Magnetic Resonance in Medicine, Vol. 67, No. 2, pp. 552 – 561, 2011.